Application of the Compressed Sensing Technique to Self-Gated Cardiac Cine Sequences in Small Animals

Paula Montesinos,[1,2]* Juan Felipe P.J. Abascal,[1,2] Lorena Cussó,[1,2,3] Juan José Vaquero,[1,2] and Manuel Desco[1,2,3]

Purpose: Self-gated cine sequences are a common choice for cardiac MRI in preclinical applications. The aims of our work were to apply the compressed sensing technique to IntraGate-FLASH cardiac MRI studies on rats and to find the maximum acceleration factor achievable with this technique.
Theory and Methods: Our reconstruction method extended the Split Bregman formulation to minimize the total variation in both space and time. In addition, we analyzed the influence of the undersampling pattern on the acceleration factor achievable.
Results: Our results show that acceleration factors of up to 15 are achievable with our technique when appropriate undersampling patterns are used. The introduction of a time-varying random sampling clearly improved the efficiency of the undersampling schemes. In terms of computational efficiency, the proposed reconstruction method has been shown to be competitive as compared with the fastest methods found in the literature.
Conclusion: We successfully applied our compressed sensing technique to self-gated cardiac cine acquisition in small animals, obtaining an acceleration factor of up to 15 with almost unnoticeable image degradation. **Magn Reson Med 000:000–000, 2013. © 2013 Wiley Periodicals, Inc.**

Key words: compressed sensing; self-gated; total variation; Split Bregman; undersampling pattern; cardiac cine MRI

INTRODUCTION

Different types of cardiac cine sequences are widely used to assess cardiac function, evaluate heart motility, and quantify ejection fraction, both in clinical and pre-clinical applications. Several of these cine sequences can use prospective or retrospective gating. With prospective gating, the electrocardiograph (ECG) signal is used to synchronize image acquisition with the cardiac cycle, while the respiration signal is used to avoid motion artifacts by interrupting the acquisition at specific moments of the respiratory cycle. One drawback of prospective gating is that the use of electrodes at high fields is challenging and prone to artifacts, particularly in small-animal studies. Retrospective cardiac gating obviates the need for ECG by means of a continuous acquisition that is retrospectively sorted into different cardiac phases based on navigator echoes that allow generating cardiac and respiratory synchronism signals. IntraGateFLASH (1) is a self-gated FLASH (fast low angle shot), an example of a self-gated fast gradient echo sequence, in which a navigator echo is stored with each phase encoding line. According to its corresponding navigator signal, the different phase encodings are retrospectively sorted and averaged to arrange several complete k-spaces (Fig. 1).

In cardiovascular applications, acquisition time is directly related to the spatiotemporal resolution and signal-to-noise ratio (SNR) of the reconstructed images. Several acceleration methods enable faster acquisitions (or higher quality images, if acquisition time is maintained). In the last few years, good results for cardiac MRI have been reported with methods such as UNFOLD (2), k-t BLAST and k-t SENSE (3), PARADIGM (4), k-t SPARSE (5), k-t FOCUSS (6), k-t PCA (7), PSF model based reconstruction (8–10), k-t ISD (11), and k-t SLR (12). Many other methods have also been reported (13–19).

The compressed sensing (CS) paradigm states that an exact image reconstruction can be achieved from randomly undersampled data using an appropriate nonlinear approach, if we can assume that the image has a sparse representation in the pixel space or in any other transformed domain (20,21). The quality of the reconstruction depends on the degree of data undersampling and image sparsity, and on the particular nonlinear reconstruction algorithm used (22).

Some images may actually be sparse in terms of their spatial representation, as is the case in angiographic studies. In other situations, the most common approach is to use the image gradient as the transform domain. If a sparse solution exists, it can be found by minimizing the L1 norm of the image gradient, also known as total variation (TV). In dynamic applications (where a temporal dimension is involved), we can exploit both spatial and temporal sparsity, because consecutively acquired images are expected to show a strong correlation. Hence it is possible to minimize the TV across both the spatial and temporal dimensions, as we propose in this work.
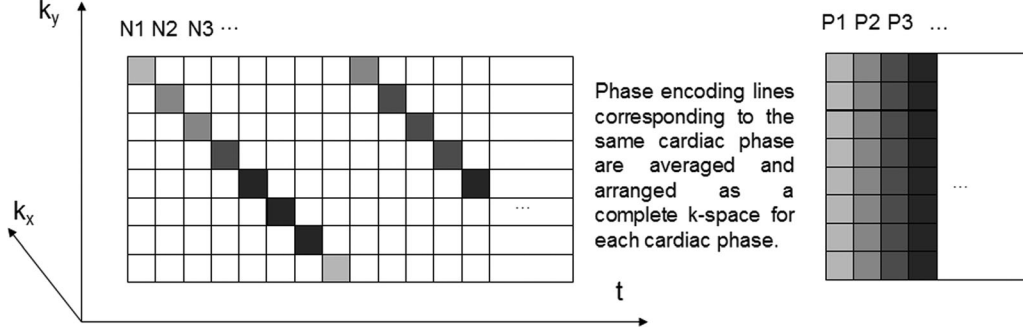
FIG. 1. IntraGateFLASH acquisition scheme.

For dynamic applications, the magnitude of the CS problem could increase considerably and require computationally intensive calculations. Among the wide variety of reconstruction algorithms available, the Split Bregman method and similar procedures (23–26) have proved to be more computationally efficient than classic optimization methods for solving problems with L1-functionals, especially for the minimization of spatial TV. Although the Split Bregman methodology has already been successfully applied in static MRI images (27–30), the potential advantages of a spatiotemporal approach have not been yet evaluated.

Most previous dynamic CS approaches to human cardiac MRI focused on prospective cine acquisitions; only two included retrospective classifications (6,19). Few previous works are available on small-animal preclinical applications (9,16,31–33) and only a very recent study has addressed the use of retrospective self-gated cine sequences (33).

The aims of our work were to apply the CS technique to IntraGateFLASH cardiac MRI studies on rats and to find the maximum acceleration factor achievable with this technique. One of the contributions of this study is to extend the Split Bregman formulation to minimize the TV in both the spatial and the temporal dimensions. In addition, we propose a new framework for analyzing the effect of the undersampling pattern on the achievable acceleration factor.

THEORY

Compressed Sensing and Split Bregman

Compressed sensing formulates the following constrained optimization problem:

$$\min_{u} \ \|\Psi u\|_1 \text{ such that } \|\tilde{F}u - f\|_2^2 < \sigma^2 \qquad [1]$$

where $\|\cdot\|_1$ is the L1-norm, Ψ denotes the linear operator that transforms the image from the pixel representation into a sparse representation, $\|\tilde{F}u - f\|_2^2 < \sigma^2$ is the data fidelity term, $\tilde{F}$ represents the undersampling Fourier operator, f represents the measured k-space, u is the image in the pixel representation and σ^2 is the variance of the signal noise. The undersampling Fourier transform can be expressed as the product of a full Fourier operator

F and a matrix R, whose role is to select the points of k-space that will be sampled or preserved ($\tilde{F} = RF$).

If we use the spatial derivatives of the images as the transform domain, $\Psi = \nabla$, where $\nabla = (\nabla_x, \nabla_y)$ is the gradient, ∇_x and ∇_y are spatial derivatives, then in Eq. [1], it will be necessary to minimize the TV of the images. Spatial TV can be computed using an anisotropic TV model (23,34,35)

$$\|(\nabla_x u, \nabla_y u)\|_1 = \|\nabla_x u\|_1 + \|\nabla_y u\|_1 \qquad [2]$$

or using an isotropic TV model (23,34,35)

$$\|(\nabla_x u, \nabla_y u)\|_2 = \sum_{i,j} \sqrt{(\nabla_x u_{i,j})^2 + (\nabla_y u_{i,j})^2} \qquad [3]$$

As L1-based CS algorithms can be computationally intensive, there is increasing interest in novel algorithms that perform faster reconstructions, such as computationally efficient orthogonal matching pursuit (13), forward-backward splitting methods (15), and first-order approximations (36,37). Among these, the so-called splitting methods decouple L1 and L2 functionals and minimize them separately, allowing the L1 subproblem to be efficiently solved using shrinkage formulas and the L2 subproblem to be solved analytically. Bregman iteration technique makes the solution of unconstrained problems to optimally converge to equivalent constrained problems (23,24,26,38). Based on Bregman iteration method, Split Bregman solves the constrained problem exactly for convex nondifferentiable functionals such as TV (23).

Extension of the Split Bregman Technique to MRI Spatiotemporal Models

Based on the inherent similarity between frames in a cine acquisition, we extend the formulation from Eq. [1] to minimize the TV both in space and in time (39). Using an isotropic spatial TV model, we obtain the following constrained optimization problem:

$$\min_{u} \ \|(\nabla_x u, \nabla_y u)\|_2 + \|\nabla_t u\|_1 \text{ such that } \|RFu - f\|_2^2 < \sigma^2$$
$$[4]$$

where ∇_t is the temporal derivative (see Figure 2) and $\|\nabla_t u\|_1$ is the temporal TV.
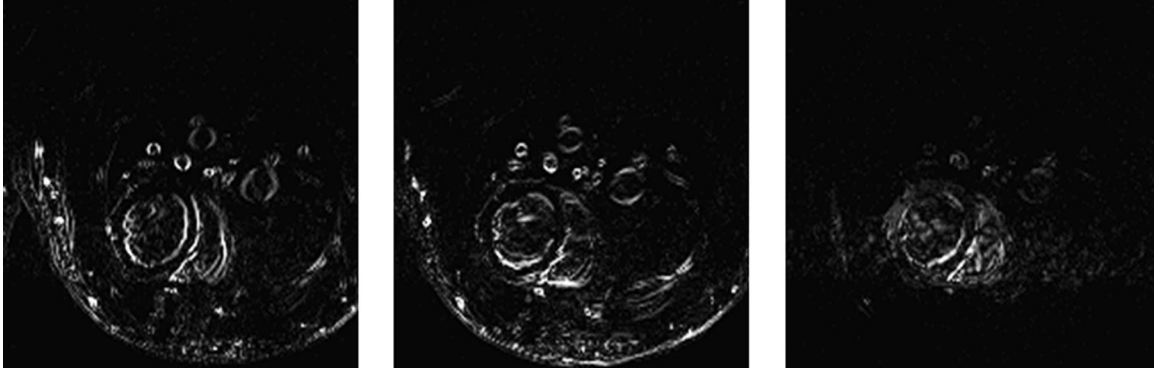
FIG. 2. Spatial and temporal gradients: from left to right $\|Dx\|$, $\|Dy\|$, and $\|Dt\|$.

Taking the spatial formulation introduced by Goldstein (23) as our starting point, we can expand the Split Bregman formulation to both spatial and temporal domains. We introduce the new complex-valued variables d_x, d_y, and d_t that allow the splitting of L1 and L2 functionals. Making the replacements $d_x \leftarrow \nabla_x u$, $d_y \leftarrow \nabla_y u$, and $d_t \leftarrow \nabla_t u$ the problem in Eq. [4] is reformulated as:

$$\min_{d_x,d_y,d_t,u} \; \left\|(d_x, d_y)\right\|_2 + \; \left\|d_t\right\|_1 \text{ such that } \left\|RFu - f\right\|_2^2 < \sigma^2,$$
$$d_i = \nabla_i u, i = x, y, t \quad [5]$$

This constrained problem can be solved by using an equivalent unconstrained problem based on Bregman iterations (23). By applying the Bregman iterations, represented by b_i^k and f^k, the following unconstrained formulation converges iteratively to the constrained problem in Eq. [5].

$$\min_{d_x,d_y,d_t,u} \; \left\|(d_x, d_y)\right\|_2 + \; \left\|d_t\right\|_1 + \frac{\mu}{2}\left\|RFu - f^k\right\|_2^2$$
$$+ \frac{\lambda}{2}\left\|d_x^k - \nabla_x u - b_x^k\right\|_2^2 + \frac{\lambda}{2}\left\|d_y^k - \nabla_y u - b_y^k\right\|_2^2$$
$$+ \frac{\lambda}{2}\left\|d_t^k - \nabla_t u - b_t^k\right\|_2^2$$
$$[6]$$

where λ is a constant penalty weighting parameter for the TV constraints and μ is a constant penalty weight parameter for the data fidelity term.

At each iteration k, Bregman iterations define a new problem in which the variables u^k and d_i^k are updated and exactly solved; constraints are imposed by adding the error back into the constraint in each iteration:

$$b_i^{k+1} = b_i^k + (\nabla_i u^{k+1} - d_i^{k+1}) \; .$$
$$f^{k+1} = f^k + f - RFu^{k+1} \quad [7]$$

For a large number of iterations, and for parameters λ and μ sufficiently small, the constraints are imposed iteratively in a smooth way and the Bregman iterations lead to a sequence of solutions u^k that will get monotonically close to a solution of the original constrained problem, u, while the data fidelity term monotonically decreases to zero (26).

In fact, as long as the weighting parameters are small, and the number of iterations is large, the influence of these parameters is small (23,38). Thus, there is no need to carefully optimize the weighting parameters, as opposed to unconstrained optimization problems, where regularization parameters have to be cautiously selected (for example with the L-curve method). This is an additional advantage of the Split Bregman formulation. The most important of these two parameters is μ, that weights the data constraint and thus affects the convergence speed. Higher values of μ speed up convergence, although it must remain sufficiently small to guarantee convergence (38). Usually λ and μ are chosen empirically (23).

As u and d_i are independent (see Eq. [6]), they can be split into two subproblems and solved separately. We address first the solution of μ which is obtained by solving the following L2-norm subproblem:

$$u^{k+1} = \min_u \; \frac{\mu}{2}\left\|RFu - f^k\right\|_2^2 + \frac{\lambda}{2}\left\|d_x^k - \nabla_x u - b_x^k\right\|_2^2 +$$
$$+ \frac{\lambda}{2}\left\|d_y^k - \nabla_y u - b_y^k\right\|_2^2 + \frac{\lambda}{2}\left\|d_t^k - \nabla_t u - b_t^k\right\|_2^2. \quad [8]$$

As this subproblem is differentiable, by differentiating with respect to u and setting the result equal to zero, we obtain the update rule,

$$K \cdot u^{k+1} = r^k \quad [9]$$

where

$$K = (\mu F^T R^T RF + \lambda \nabla_x^T \nabla_x + \lambda \nabla_y^T \nabla_y + \lambda \nabla_t^T \nabla_t) \quad [10]$$

and

$$r^k = \mu F^T R^T f^k + \lambda \nabla_x^T (d_x^k - b_x^k) + \lambda \nabla_y^T (d_y^k - b_y^k) + \lambda \nabla_t^T (d_t^k - b_t^k). \quad [11]$$

Equation [9] can be further simplified by means of $\nabla^T \nabla = -\Delta$ for a definition of ∇ including all the derivatives $\nabla = (\nabla_x, \nabla_y, \nabla_t)$ leading to the following expression:

$$(\mu F^T R^T RF - \lambda \Delta)u^{k+1} = r^k. \quad [12]$$

This involves solution of the linear system in the image domain $K(x,t)u(x,t) = r(x,t)$. This approach is computationally very expensive, as it requires the inversion of a matrix K of

size $(N_x N_y N_t)^2$. To avoid this inversion, Eq. [12] can be rewritten in the Fourier domain as done in (23,35), $\hat{K}(k,v)\hat{u}(k,v) = \hat{r}(k,v)$. This only requires a pixel-by-pixel operation of size $N_x N_y N_t$ and three Fourier transforms, two three-dimensional (3D) fast Fourier transform (FFT) for inverting the linear system and one frame-by-frame 2D FFT to compute the first term of the right-hand side of Eq. [11]. The Fourier formulation can only be implemented when all the mathematical operators in Eq. [12] have a Fourier representation. In our case, because all the derivative operators are analytical functions in the Fourier domain, we can take advantage of working in the Fourier domain and thus substantially reduce the computational burden of the problem. While the previous Fourier formulation has been shown to be computationally efficient in 2D (23), the present study is the first to show the greater benefit obtained in 3D problems.

The Fourier 3D formulation can be implemented by representing all variables and mathematical operators in 3D (size $N_x N_y N_t$) and solving Eq. [12] as

$$u^{k+1} = F_{3D}^{-1}[F_{3D}(r^k)./\hat{K}_{3D}]$$ [13]

where $\hat{K}_{3D}$ in the Fourier domain is represented as

$$\hat{K} = \mu R - \lambda \hat{\Delta}_{3D}$$ [14]

where $F^T R^T R F$ is R in the Fourier domain and $\hat{\Delta}_{3D}$ is the 3D spatial Laplacian operator in the Fourier domain. $\hat{\Delta}_{3D}$ can be implemented by taking a 3D FFT of the discrete Laplacian kernel written in the following form:

$$\text{first plane} = \begin{pmatrix} 0 & -1 & 0 \\ -1 & 6 & -1 \\ 0 & -1 & 0 \end{pmatrix}$$

$$\text{second plane} = \begin{pmatrix} 0 & 0 & 0 \\ 0 & -1 & 0 \\ 0 & 0 & 0 \end{pmatrix}$$

$$\text{last plane} = \begin{pmatrix} 0 & 0 & 0 \\ 0 & -1 & 0 \\ 0 & 0 & 0 \end{pmatrix}.$$ [15]

This implementation is an extension from the 2D version of the Split Bregman method provided by Goldstein's code (Split Bregman, http://tag7.web.rice.edu/Split_Bregman.html).

On the other hand, splitting variables d_i can be derived from Eq. [6] and solved using generalized shrinkage formulas (24,35)

$$d_t^{k+1} = \min_{d_t} \|d_t\|_1 + \frac{\lambda}{2}\|d_t^k - \nabla_t u^{k+1} - b_t^k\|_2^2$$ [16]

$$d_t^{k+1} = \text{shrink}(\nabla_t u^{k+1} + b_t^k, 1/\lambda)$$ [17]

$$\text{shrink}(x, \gamma) = \frac{x}{|x|} * \max(|x| - \gamma, 0).$$ [18]

In the case of d_x^{k+1}, d_y^{k+1} we use an isotropic shrinkage formula

$$(d_x^{k+1}, d_y^{k+1}) = \min_{d_x, d_y} \|(d_x, d_y)\|_2 + \frac{\lambda}{2}\|d_x^k - \nabla_x u^{k+1} - b_x^k\|_2^2$$
$$+ \frac{\lambda}{2}\|d_y^k - \nabla_y u^{k+1} - b_y^k\|_2^2$$ [19]

$$d_x^{k+1} = \max(s^k - 1/\lambda, 0)\frac{\nabla_x u^{k+1} + b_x^k}{s^k}$$ [20]

$$d_y^{k+1} = \max(s^k - 1/\lambda, 0)\frac{\nabla_y u^{k+1} + b_y^k}{s^k}$$ [21]

$$s^k = \sqrt{|\nabla_x u^{k+1} + b_x^k|^2 + |\nabla_y u^{k+1} + b_y^k|^2}$$ [22]

The complete algorithm that solves the constrained optimization problem in Eq. [4], for given values of λ and μ, is shown below:

Initialize : $f^0 = f$, and $d_x^0 = d_y^0 = b_x^0 = b_y^0 = 0$

$\hat{K} = \mu R - \lambda \hat{\Delta}_{3D}$

While $\|RFu^k - f\|_2^2 > \sigma^2$

Loop N times

$r^k = \mu F^T R^T f^k + \lambda \nabla_x^T(d_x^k - b_x^k) + \lambda \nabla_y^T(d_y^k - b_y^k) + \lambda \nabla_t^T(d_t^k - b_t^k)$

$u^{k+1} = F^{-1}[\hat{r}^k./\hat{K}]$

$d_t^{k+1} = \text{shrink}(\nabla_t u^{k+1} + b_t^k, 1/\lambda)$

$b_t^{k+1} = b_t^k + (\nabla_t u^{k+1} - d_t^{k+1})$

$s^k = \sqrt{|\nabla_x u^{k+1} + b_x^k|^2 + |\nabla_y u^{k+1} + b_y^k|^2}$

$d_x^{k+1} = \max(s^k - 1/\lambda, 0) \frac{\nabla_x u^{k+1} + b_x^k}{s^k}$

$d_y^{k+1} = \max(s^k - 1/\lambda, 0) \frac{\nabla_y u^{k+1} + b_y^k}{s^k}$

$b_x^{k+1} = b_x^k + (\nabla_x u^{k+1} - d_x^{k+1})$

$b_y^{k+1} = b_y^k + (\nabla_y u^{k+1} - d_y^{k+1})$.

end

$f^{k+1} = f^k + f - RFu^{k+1}$

end

We tested different values of N, ranging from 1 to 50, where N is the number of iterations of the inner loop in charge of imposing the TV restriction. N = 1 proved to be empirically optimum (40).

In conclusion, Split Bregman divides the reconstruction problem into two subproblems: a quadratic problem that is exactly and efficiently solved in the Fourier domain; and a second problem that includes all the L1-norm functionals solved using shrinkage operations. To our knowledge, we present the first implementation of a CS method using a complete Split Bregman formulation in the Fourier domain to minimize the TV in both space and time in dynamic MRI studies.

METHODS

Data Sets

The results presented in this work were obtained by simulating different undersampling patterns over real acquired
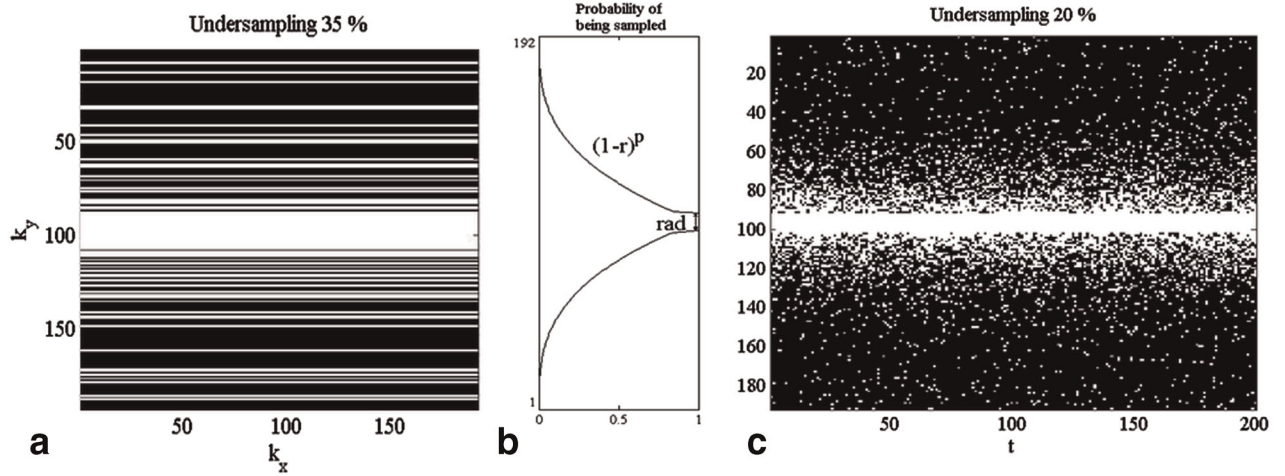
FIG. 3. **A:** k_x-k_y undersampling pattern. **B:** Probability density function. **C:** k-t undersampling pattern.

data from small-animal MRI studies (rat cardiac cine sequences).

The original datasets were acquired with a 7 Tesla (T) Bruker Biospec 70/20 scanner using a linear coil resonator for transmission and a dedicated four-element cardiac phased array coil for reception. The IntraGateFLASH sequence used had the following parameters: echo time (TE) = 2.43 ms, repetition time (TR) = 8 ms, number of total repetitions = 200, number of frames = 8, matrix size = 192 × 192, field of view = 4.8 × 4.8 cm, and slice thickness = 1.2 mm. A total of 192 × 200 correlative phase encodings were acquired in a total time of 5 min 7 s. Although a TR of 8 ms could theoretically lead to 15–16 frame cine movies, the retrospective character of our acquisition allowed us to decide a posteriori the number of cardiac frames during the reconstruction process. After several experiments and reconstructions, and based on a reasonable acquisition time and SNR values, we decided that eight was the optimal number of frames for our study.

After the simulated undersampling patterns were applied to the complete data sets, the phase encodings were retrospectively classified into eight complete k-spaces, one for each desired time frame. The reconstructions were performed separately for each element of the phased array and subsequently combined with a sum of squares.

Data from four female Wistar rats (weight ranging from 250 g to 350 g) were used for the assessment of feasible acceleration factors. Animals were treated according to the European Communities Council Directive (86/609/EEC) and with the approval of the Animal Experimentation Ethics Committee of Hospital General Universitario Gregorio Marañón.

Undersampling Pattern

An appropriate selection of undersampling patterns intended for each application is essential. First, it is important to consider the specific timing of the sequence involved. For the IntraGateFLASH sequence, acquisition time is directly proportional to the number of acquired phase encodings; therefore, to achieve a reduction in acquisition time, it is necessary to remove complete phase encoding lines from the acquisition scheme. In addition, a random undersampling scheme fulfills the requirement of producing incoherent artifacts, as required by the CS theory (22).

Lustig et al suggested to make use of quasi-random patterns following a Monte Carlo procedure based on a variable probability density function (22). By adapting their methodology to the requirements set out above, we created a polynomial probability density function (Eq. [23]) that assigned different sampling probabilities to different regions of k-space. Two user-selectable parameters make it possible to choose several lines in the center of the k-space, which will always be sampled, and to select the probability decay rate with which the remaining phase encodings will be sampled, as a function of its distance to the center of the k-space (Fig. 3B).

$$\begin{cases} (1-r)^p & if \quad |r| \geq rad \\ 1 & if \quad |r| < rad \end{cases} \quad [23]$$

Lustig et al suggested the use of the TPSF (Transform Point Spread Function) to select appropriate undersampling patterns (22). Because TPSF measures propagation error, the best patterns are those with a low TPSF. Lustig et al proposed repeating the generation process several times to create different undersampling patterns and to select that with the lowest TPSF. In our work, we go beyond TPSF criterion, which alone is not robust enough to select good undersampling patterns.

For our IntraGateFLASH application, we tested and compared two undersampling patterns, k_x-k_y and k-t.

k_x-k_y Pattern

The k_x-k_y pattern is the simpler of the two. Randomization is performed only in the phase encoding direction (Fig. 3A), and the same phase encoding lines are removed throughout the acquisition period. Thus, this

approach is equivalent to applying the same k_x-k_y undersampling pattern to all the final cardiac frames.

Before selecting the undersampling patterns, we tested whether the TPSF criterion alone was adequate for our k_x-k_y patterns. To this end, we generated 500 patterns using a function from Lustig's original undersampling code (22). Each call to this function generates 10 random patterns and returns the one with the lowest TPSF value. We repeated the call 500 times to produce the 500 undersampling patterns used in our work.

We also tested whether the suitability of the undersampling patterns was independent from the cardiac frame we were working with. Therefore, 50 different patterns were applied over the two most different cardiac frames, namely, those corresponding to the cardiac diastole and systole. The errors obtained over these two different frames were compared.

k-t Pattern

In this case, the undersampling pattern applied during the acquisition changes randomly over time, thus making it possible to perform randomization both in the phase encoding and in the temporal dimensions (Fig. 3C). After undersampling, the data are classified according to their navigator signals and averaged into the final cardiac frames; this approach is equivalent to using a different random k_x-k_y pattern (Fig. 3A) for each final frame. Figure 1 illustrates how each line of the final k-spaces is the average of a specific number of actually acquired k-space lines; the number of averaged lines depends on the navigator signal, which in turn depends on cardiac movement during acquisition. Therefore, we are only able to establish the undersampling k-t pattern that will be executed during the acquisition, whereas the resultant k_x-k_y patterns obtained after the averaging step cannot be determined in advance.

One advantage of this kind of pattern combined with the IntraGateFLASH sequence is that, thanks to the data averaging step, the percentage of nonzero data in the final k-space of each frame will be higher than the percentage actually applied during acquisition. As an example, one of the undersampling patterns we tested preserved only 15% of the original acquired data; however, after sorting and averaging, the percentage of nonzero data in the eight final k-spaces filled 27% of the eight final frames. Henceforth, the term "data percentage" refers to the percentage of data actually acquired which correlates with the reduction in acquisition time, and does not reflect the final percentage of the k-space that is zero-filled.

As in our IntraGateFLASH application the final k_x-k_y undersampling patterns cannot be predicted in advance, the only possibility of optimization is to vary the parameters of the probability density function used to generate the k-t undersampling pattern. We studied the influence of three parameters: the percentage of original data preserved, the exponent of the probability decay rate, and the radius, which defines the number of lines around the k-space center, which will always be fully sampled (Eq. [21]). We performed simulations by varying the percentages of maintained original data from 10% to 40%, the exponent ratio from 3 to 9, and the radius (expressed as

normalized distance to the center) from 0 to 0.1. These ranges were determined by excluding those values that clearly showed bad results after a coarse assessment of the undersampling patterns.

Maximum Acceleration Factor Achievable

The ultimate goal of this work was to find the maximum acceleration factor achievable for the cardiac cine application using our CS scheme. Different reconstructions using k_x-k_y and k-t undersampling patterns were obtained by maintaining the percentages of the original data from 10% to 40%, in 5% steps. To evaluate the influence of the number of frames (and thus indirectly the influence of the SNR level) on the acceleration factor achievable, the same dataset with k-t undersampling patterns was also reconstructed to give 16 final frames. For our fully sampled dataset using 16 frames instead of 8 suggests an SNR reduction of 1.65 times.

We implemented our reconstructions in MATLAB (MathWorks, MA, USA) on a Dell Precision T5500 with Intel Xeon, using eight CPUs (2.4 GHz and 12 GB RAM). As for the values of the weighting parameters λ and μ, we empirically tested a range from 10^{-2} to 10.

Quality Criteria

Several criteria were used to assess image quality. The first was relative reconstruction error, which was referenced to the fully sampled image (Eq. [23]).

$$error = \frac{\sqrt{\sum_{i,j} \left| I_{i,j}^{rec} - I_{i,j}^{full} \right|^2}}{\sqrt{\sum_{i,j} \left| I_{i,j}^{full} \right|^2}}. \qquad [24]$$

To determine the maximum number of achievable acceleration factors, we used several quality parameters: (i) the reconstruction error calculated from a specific region of interest (ROI) of 120 $\times$ 120 pixels around the heart, (ii) intensity profiles from an interface region over the myocardium (Fig. 9); (iii) the presence of artifacts and temporal blurring in the images, and (iv) the impact of CS acceleration on representative heart measurements such as ejection fraction and left-ventricle mass (41).

To assess temporal blurring, we calculated the mean value over time of a 5 $\times$ 5 pixel ROI and represented a y-t intensity profile containing both blood and myocardium (Fig. 10).

Finally, image quality was qualitatively assessed by an experienced cardiac MRI specialist who was blind to the method used.

All the analysis mentioned above was performed on only one small-animal dataset. Based on that analysis a range of acceleration factors was considered as feasible for this application. To verify its reproducibility, those acceleration factors were also simulated on a total of four small-animal datasets. To evaluate the impact of the obtained accelerations on functional parameters, the following single-slice functional measurements were performed: (i) percentage difference between end-diastolic
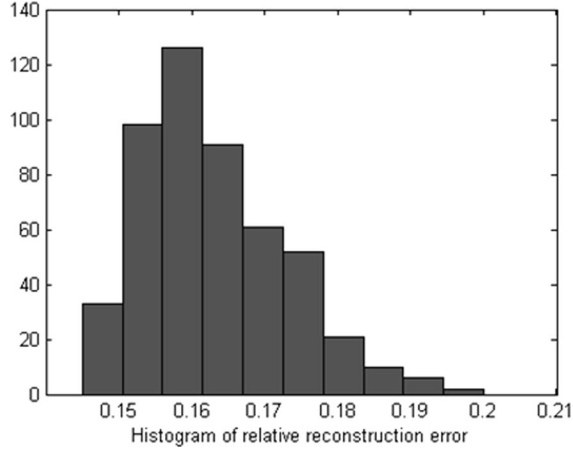
FIG. 4. Histogram of the reconstructed error of 500 random patterns, maintaining 20% of the original data.

and end-systolic volumes and (ii) the left ventricle mass measured in diastole, both of them referred to the slice. The hearts were manually segmented by an experienced specialist.

$$\% \, volume \, difference = \frac{EDV - ESV}{EDV} \quad [25]$$

$$Slice \, mass = \rho * (Epicardium \, area - Endocardium \, area) \\ * slice \, thickness \quad [26]$$

where EDV and ESV are the end-diastolic and end-systolic volumes respectively, and $\rho = 1.055$ g/cm^3 is the estimated density of the myocardium.

To define an acceptance range for these functional parameters we, first, estimated the intraobserver variability through the standard deviation of three measurements obtained from the fully sampled image of the first animal analyzed by an experienced observer. The acceptance range for each animal was defined as ± 2 intraobserver standard deviations from the fully sampled values (roughly, within the 95% confidence interval).

RESULTS

The following solutions were obtained using $\lambda=1$ and $\mu=4$, values that appeared to be empirically optimal.
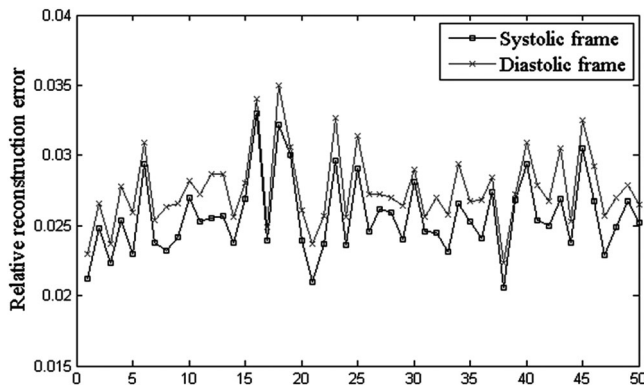

FIG. 5. Reconstruction error using 50 different single-frame patterns in systolic and diastolic frames.
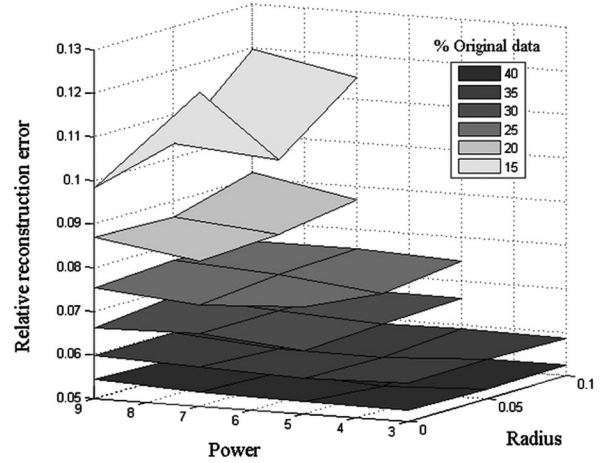

FIG. 6. Relative reconstruction error as a function of the percentage of original data maintained, the decay exponent, and the radius.

Undersampling Pattern

k_x-k_y Pattern

Figure 4 shows the relative reconstruction error yielded by the 500 patterns with low TPSF. The positive skewness of the histogram (0.71) suggests that most of the randomly generated patterns lead to low reconstruction errors. However, 24% led to an error greater than 0.17, which we considered too high.

Figure 5 shows the relative reconstruction errors of the 50 patterns measured over the systolic and diastolic frames. Although these frames differ in the image domain, they show a similar trend in the reconstruction error, thus indicating that the selection of optimal patterns is frame-independent.

k-t Pattern

Figure 6 shows relative reconstruction errors expressed as a function of the three eligible parameters of the probability density function implemented, namely, the percentage of original data preserved, the decay exponent, and the radius. The reconstruction error does not change significantly with the exponent or the radius. The results seem to depend mainly on the percentage of data, as long as we choose reasonable values for the other parameters (not a large radius for example).

Maximum Acceleration Factor Achievable

Figure 7 shows the mean squared error of reconstructed images calculated over a ROI around the myocardium for different acceleration factors and undersampling pattern types.

The end of systole frame corresponding to the maximum acceleration factors (preserving good quality image) of each pattern type are presented in Figure 8. All images have the same scale but difference images are displayed with an amplification factor of 5 to make more conspicuous the differences and the presence of artifacts.

To complete the quality assessment, intensity profiles were also drawn in the boundaries of the myocardium
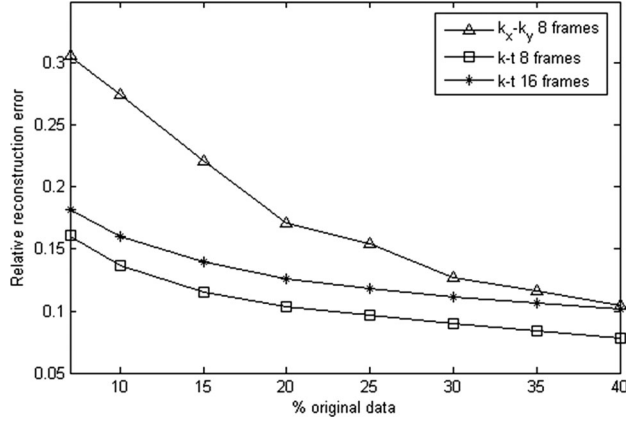
FIG. 7. Mean squared error as a function of the percentage of original data maintained.

(Fig. 9). Figure 10 shows an analysis of the temporal behavior of the reconstructed images. As expected, the application of k-t undersampling patterns offers much better results than k_x-k_y patterns in all cases. This difference is more noticeable for lower percentages of maintained data.

To evaluate the impact of acceleration on functional parameters, we analyzed the percentage difference between end-diastolic and end-systolic volumes and the within-slice left ventricle mass in the four available small-animal datasets for the higher acceleration rates (10 and 15). From the three intraobserver measurements obtained, we established the acceptable deviation range from the fully sampled image as $\pm$ 4.5% and $\pm$ 5.5 mg for the first and second functional parameters evaluated, respectively.

Both functional parameters measured for all the images reconstructed with higher acceleration factors (10 and 15) were inside the acceptable margin for the four subjects analyzed. The Table 1 shows the actual values for the four animals studied, for both the fully sampled and the reconstruction preserving only 7% of the data (A = 15).

DISCUSSION

We verified that Split Bregman reconstruction based on the minimization of the TV across both space and time is a suitable and efficient method for applying the CS technique to self-gated cardiac cine MRI sequences in rats. Undersampling patterns with randomized sampling over time enabled us to achieve acceleration factors of up to 15 before significant image degradation occurred.

Selection of Undersampling Pattern

Regarding the selection of k_x-k_y undersampling patterns, we found that using purely random patterns leads to a wide range of reconstruction errors (32% difference between the lowest and the highest error, Fig. 4), even though they comply with the low TPSF criterion. Thus, we complemented the TPSF criterion by testing the specific undersampling patterns over sample images. As shown in Figure 5, the frame-independent behavior of
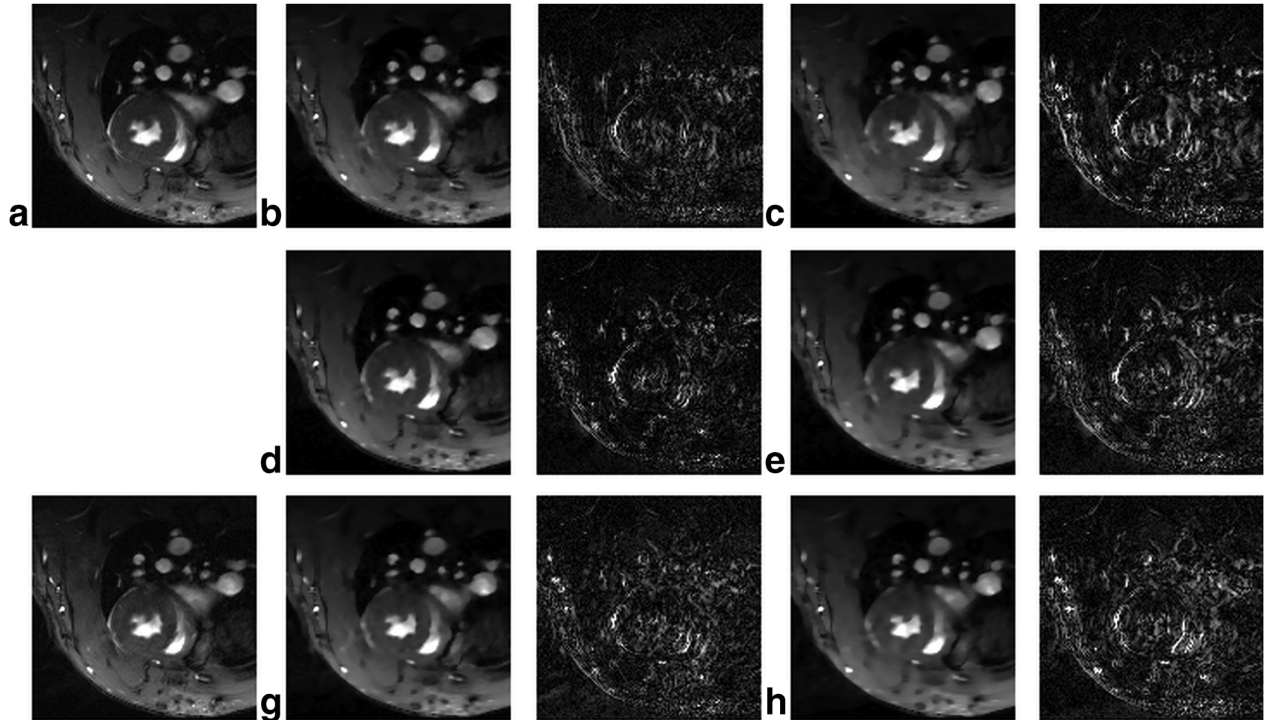

FIG. 8. Reconstructed and difference images (with an amplification factor of 5) for different undersampling patterns and acceleration factors (A), end of systole frame is shown. **A:** Fully sampled image, eight frames. **B:** The 30% k_x-k_y pattern, A=3.3. **C:** The 20% k_x-k_y pattern, A=5. **D:** The 10% k-t pattern, A = 10. **E:** The 7% k-t pattern, A = 15. **F:** Fully sampled image, 16 frames. **G:** The 10% k-t pattern, A = 10, 16 frames. **H:** The 7% k-t pattern, A = 15, 16 frames.

Table 1
Percentage Difference between End-Diastolic and End-Systolic Volumes (%V_diff) and within-Slice Left Ventricle Mass (LVM) for the Four Available Small-Animal Datasets (A, B, C, and D) for Both the Fully Sampled Image (FS) and the Compressed Sensing (CS) Images Reconstructed with k-t Patterns and 7% of the Preserved Data (A = 15)

Animal	A		B		C		D	
Type of reconstruction	FS	CS	FS	CS	FS	CS	FS	CS
% V_diff	72.3	73.1	71.8	70.33	72.41	74.03	71.64	74.96
LVM (mg)	62.8	68.34	60.07	56.56	54.42	55.54	54.75	58.56

undersampling patterns allows us to safely extrapolate from sample images to future cardiac studies.

For the k-t pattern, the most influential parameter is the undersampling percentage. The fact that final k-spaces are obtained from averaged data seems to alleviate the influence of a high decay exponent or the radius of the probability density function.

Maximum Acceleration Factor Achievable

As expected, k_x-k_y undersampling patterns lead to lower acceleration factors (around 3) than a randomization performed over time (between 10 and 15). A key fact of our implementation is that the benefits of using randomization over time are boosted by the data-averaging step, as the percentage of nonzero data in the final k-space of each frame is higher than the percentage actually applied during acquisition.

Selection of the optimal undersampling percentage is very dependent on tolerance to artifacts in the final image. The k-t pattern with a factor of 15 still led to good quality reconstructions, although the intensity profiles over the myocardium were sharper for lower acceleration factors (Fig. 9). As for temporal behavior, some blurring appears at accelerations higher than 3 for the k_x-k_y patterns and 7 for the k-t patterns. However, the presence of some artifacts due to high undersampling rates, as in Figures 8C and 8D does not necessarily alter the end diastolic and end systolic volumes neither the endocardium and epicardium areas measured in the images. According to the subjective assessment of an expert, factors of up to 5 produced no noticeable change in the images. Beyond this point, image quality decreased with the undersampling percentage, although it was still considered acceptable for factors up to 10 or 15. This statement is reinforced by the functional measurements on four animals, which were still in agreement with the values obtained from its respectively fully sampled images.

Regarding the influence of the number or frames (or SNR) on the final achievable acceleration factor, Figure 7 shows how as the SNR decreases, the reconstruction
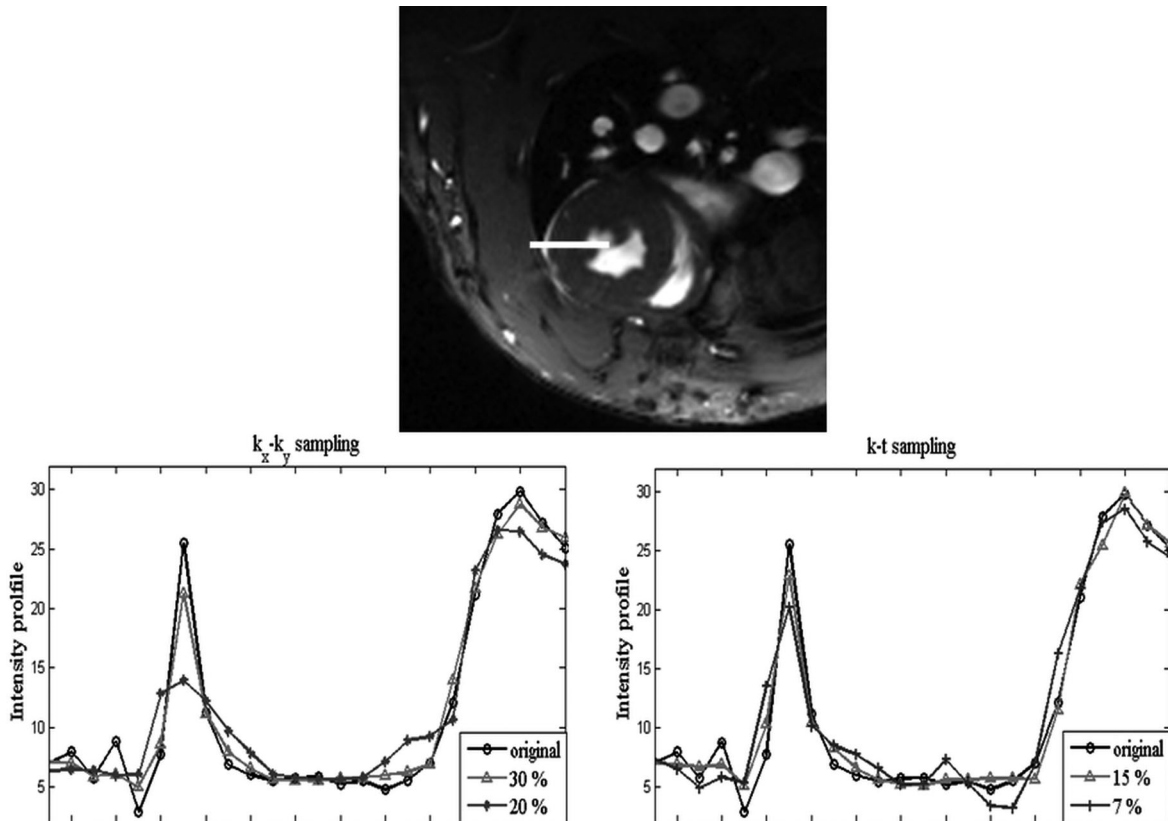

FIG. 9. Intensity profiles. **A:** k_x-k_y undersampling pattern. **B:** k-t undersampling pattern.
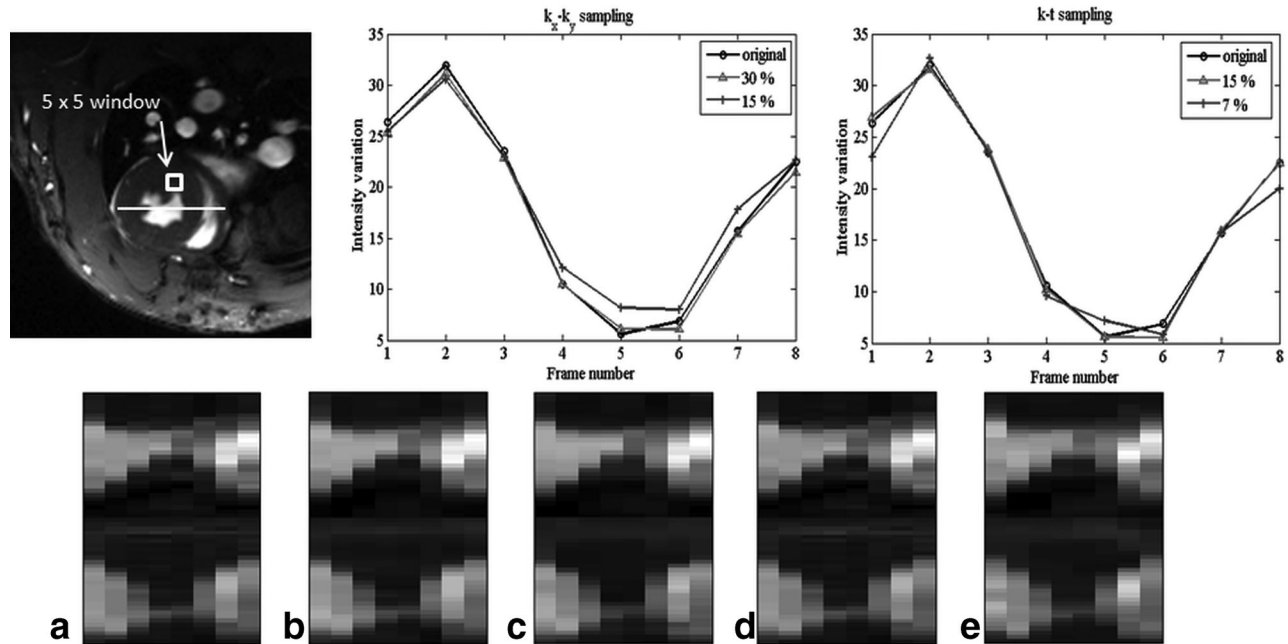
FIG. 10. Analysis of temporal blurring. Top row: mean value in 5 × 5 pixels ROI, for k_x-k_y undersampling pattern and k-t undersampling pattern. Bottom row: **A:** Fully sampled image. **B:** The 30% k_x-k_y pattern, A = 3.3. **C:** The 20% k_x-k_y pattern, A = 5. **D:** The 15% k-t pattern, A = 6.6. **E:** The 7% k-t pattern, A = 15.

error increases. This can be also seen in Figure 8H, where the presence of artifacts is slightly more noticeable than when using 8 frames, although the quality for 16 frames is still acceptable. Accordingly, it seems that the final acceleration factor must be selected ad hoc, depending on the quality vs. acquisition time requirements for each application and user.

The literature contains several findings on CS algorithms applied to cardiac cine sequences. Some have been applied in simulations and others to real data of human cine images, although few have been tested with small animal studies. A wide range of acceleration factors has been reported: in human cardiac studies they range from 3 (19) to 16 (15); most are around 6 or 9 (6). For small animals, reported acceleration factors are approximately 3 (16,33) or 9 when combined with GRAPPA (generalized autocalibrating partial parallel acquisition) (31); our acceleration factor of 15 is clearly an improvement on these results. We expect to obtain even higher acceleration factors in future versions of our algorithm by combining CS with parallel imaging strategies or coil spatial information.

Of interest, a simple straight comparison of acceleration factors between methods is not completely fair owing to differences in field strength, in the spatiotemporal resolution of the original images, and differences in the quality pursued in the final images. Another source of disparity is the potential difference between using prospective or retrospective cine sequences. Depending on the reconstruction used, retrospective cine sequences provide images with a higher SNR than prospective ECG cardiac cine sequences in the same acquisition time (or with the same SNR for a lower acquisition time) (1).

The only previous study that made use of retrospective cine in small-animal studies reported an acceleration factor of 3 (33), which is much lower than that achieved with our approach. We used the same basic MRI sequence and the same sparse transform, although important differences were recorded between both approaches. Motaal et al used undersampling patterns randomized over time, but they did not apply variable density functions to generate them. In addition, the approach of Motaal et al applies to the very specific case of high-frame-rate cine sequences, whereas our work is concerned with the more common case of low-frame-rate cines with higher quality images. The acquisition parameters in both works, and therefore the quality of the original fully sampled images, are very different. In our case, the higher quality of the original images enabled higher acceleration factors, thus explaining in part the large difference in the acceleration factors achieved.

Efficiency of the Reconstruction Algorithm

In our algorithm, we used temporal and spatial TV as regularization functionals. However, other regularization terms can be easily used in the Split Bregman formulation (23). For spatial regularization, spatial TV (15) and wavelet transform or a combination of both (22) are the most widely used. It is known that spatial TV removes noise and incoherent artifacts and provides stability to the reconstruction algorithm (23). For this reason it has been suggested to combine TV with other sparsity transforms, such as wavelet or curvelet transforms (42). With regard to temporal regularization, temporal TV (33), nuclear norm (12,17), 1D wavelet transform (43) or

discrete cosine transform (22) has been previously proposed.

In general, spatial and temporal TV lead to sparse representation and provides good acceleration factors, as presented in this study. However, other spatial and temporal transforms that lead to sparser representations may provide even higher acceleration factors, although sparsity is not the only requirement to get better results.

In dynamic applications, the CS problem requires computationally expensive calculations when using classic constrained and even unconstrained optimization methods. However, Split Bregman solves the constrained problem exactly and efficiently by using a splitting framework that leads to a quadratic equation (solved in the Fourier domain) and to shrinkage operations. The advantages of our reconstruction algorithm include the fact that derivative operators are analytical functions in the Fourier domain and thus allow us to avoid selecting and using a regularization parameter inherent to unconstrained problems. One of the contributions of our work is to extend and validate the benefits of the spatiotemporal Split Bregman formulation.

Our results showed that several of approximately 500 iterations is enough to achieve a reasonable quality in reconstructed images, for $\lambda=1$ and $\mu=4$. With our entire data set (32 images, 8 frames, 4 coil elements) the reconstruction was completed in 90 s on a Dell Precision T5500 with Intel Xeon, using 8 CPUs (2.4 GHz and 12 GB RAM). Our computing time per frame was competitive with the fastest method found in the literature (13) and is lower than most (16), thus confirming the computational advantages of using the Split Bregman method for spatiotemporal applications. The number of iterations, and so the reconstruction time, depends on the values of λ and μ. In our work, the values chosen were obtained after an empirical assessment. As in other studies (23,38) the accuracy of the solution was not very sensitive to the actual value of these parameters, yet the value of μ affects the reconstruction time. It is possible that the optimum value might be different for other type of studies (for instance, different anatomical localization or spatiotemporal resolution).

Limitations and Future Work

It is important to note that the results of our work were based on simulations performed using real data in which the undersampling patterns where applied a posteriori over the fully sampled acquired data. Initial real experiments acquired in CS regimen suggest that acceleration factors of around 10 are easily achievable. Work in progress is focused on increasing this acceleration factor, reducing the artifacts present in the images. A detailed study with a higher sample of subjects to assess the acceleration factor advisable for routine preclinical studies is warranted. This study should cover whole heart cine acquisitions on animals with different physiological characteristics (such as different motility or different cardiac frequency). Whole ventricle ejection fraction (EF) and left-ventricle mass measurements (LVM) should be performed and analyzed on this wide range of acquisitions. Also a specific quality control evaluating both

healthy and unhealthy cases still remains to be performed.

CONCLUSIONS

We successfully applied the CS technique to self-gated cardiac cine acquisition in small animals. For that purpose, we developed a modification of the Split Bregman reconstruction algorithm based on the minimization of TV in both spatial and temporal dimensions. The introduction of a time-varying random sampling clearly improved the efficiency of the undersampling schemes. For the specific case of IntraGateFLASH cardiac cine acquisition, the CS methodology described enabled us to obtain accelerations of up to factor 15 with almost unnoticeable image degradation.

ACKNOWLEDGMENTS

REFERENCES

1. Bovens SM, Boekhorst B, den Ouden K, van de Kolk KWA, Nauerth A, Nederhoff MGJ, Pasterkamp G, ten Hove M, van Echteld CJA. Evaluation of infarcted murine heart function: comparison of prospectively triggered with self-gated MRI. NMR Biomed 2011;24:307–315.
2. Madore B, Glover GH, Pelc NJ. Unaliasing by fourier-encoding the overlaps using the temporal dimension (UNFOLD), applied to cardiac imaging and fMRI. Magn Reson Med 1999;42:813–828.
3. Tsao J, Boesiger P, Pruessmann KP. k-t BLAST and k-t SENSE: dynamic MRI with high frame rate exploiting spatiotemporal correlations. Magn Reson Med 2003;50:1031–1042.
4. Aggarwal N, Bresler Y. Patient-adapted reconstruction and acquisition dynamic imaging method (PARADIGM) for MRI. Inverse Probl 2008;24:29.
5. Lustig M, Santos JM, Donoho D, Pauly JM.k-t SPARSE: high frame rate dynamic MRI exploiting spatio-temporal sparsity. In Proceedings of the 14th Annual Meeting of ISMRM, Seattle, Washington, USA, 2006. Abstract 2420.
6. Jung H, Sung K, Nayak KS, Kim EY, Ye JC. k-t FOCUSS: a general compressed sensing framework for high resolution dynamic MRI. Magn Reson Med 2009;61:103–116.
7. Pedersen H, Kozerke S, Ringgaard S, Nehrke K, Kim WY. k-t PCA: temporally constrained k-t BLAST reconstruction using principal component analysis. Magn Reson Med 2009;62:706–716.
8. Brinegar C, Haosen Z, Wu YJL, Foley LM, Hitchens TK, Qing Y, Pocci D, Fan L, Chien H, Zhi-Pei L. Real-time cardiac MRI using prior spatial-spectral information. Conf Proc IEEE Eng Med Biol Soc 2009; 2009:4383–4386.
9. Christodoulou AG, Brinegar C, Haldar JP, Zhang H, Wu YJL, Foley LM, Hitchens TK, Ye Q, Ho C, Liang ZP. High-resolution cardiac MRI using partially separable functions and weighted spatial smoothness regularization. Conf Proc IEEE Eng Med Biol Soc 2010;2010:871–874.
10. Zhao B, Haldar JP, Liang ZP. PSF model-based reconstruction with sparsity constraint: algorithm and application to real-time cardiac MRI. Conf Proc IEEE Eng Med Biol Soc 2010;2010:3390–3393.
11. Dong L, DiBella EVR, Rong-Rong C, Ying L.K-T ISD: compressed sensing with iterative support detection for dynamic MRI. In Proceedings of the IEEE International Symposium on Biomedical Imaging: from Nano to Macro, Chicago, Illinois, USA 2011.
12. Lingala SG, Hu Y, DiBella E, Jacob M. Accelerated dynamic MRI exploiting sparsity and low-rank structure: k-t SLR. IEEE Trans Med Imaging 2011;30:1042–1054.
13. Usman M, Prieto C, Odille F, Atkinson D, Schaeffter T, Batchelor PG. A computationally efficient OMP-based compressed sensing reconstruction for dynamic MRI. Phys Med Biol 2011;56:N99–N114.

14. Usman M, Prieto C, Schaeffter T, Batchelor PG. k-t Group sparse: a method for accelerating dynamic MRI. Magn Reson Med 2011;66: 1163–1176.

15. Montefusco LB, Lazzaro D, Papi S, Guerrini C. A fast compressed sensing approach to 3D MR image reconstruction. IEEE Trans Med Imaging 2011;30:1064–1075.

16. Wech T, Lemke A, Medway D, Stork LA, Lygate CA, Neubauer S, Kostler H, Schneider JE. Accelerating cine-MR imaging in mouse hearts using compressed sensing. J Magn Reson Imaging 2011;34: 1072–1079.

17. Goud S, Hu Y, Jacob M.Real-time cardiac MRI using low-rank and sparsity penalties. In Proceedings of the 7th IEEE International Symposium on Biomedical Imaging: from Nano to Macro, Rotterdam, the Netherlands, 2010. p 988–991.

18. Otazo R, Kim D, Axel L, Sodickson DK. Combination of compressed sensing and parallel imaging for highly accelerated first-pass cardiac perfusion MRI. Magn Reson Med 2010;64:767–776.

19. Moghari MH, Akcakaya M, O'Connor A, et al. Compressed-Sensing Motion Compensation (CosMo): a joint prospective-retrospective respiratory navigator for coronary MRI. Magn Reson Med 2011;66: 1674–1681.

20. Candes EJ, Romberg J, Tao T. Robust uncertainty principles: exact signal reconstruction from highly incomplete frequency information. IEEE Trans Inf Theory 2006;52:489–509.

21. Donoho DL. Compressed sensing. IEEE Trans Inf Theory 2006;52: 1289–1306.

22. Lustig M, Donoho D, Pauly JM. Sparse MRI: the application of compressed sensing for rapid MR imaging. Magn Reson Med 2007;58: 1182–1195.

23. Goldstein T, Osher S. The split Bregman method for L1-regularized problems. SIAM J Imaging Sci 2009;2:323–343.

24. He L, Chang T-C, Osher S, Fang T, Speier P. MR image reconstruction from undersampled data by using the iterative refinement procedure. PAMM 2007;7:1011207–1011208.

25. Cai JF, Osher S, Shen ZW. Split Bregman methods and frame based image restoration. Multiscale Model Simul 2009;8:337–369.

26. Osher S, Burger M, Goldfarb D, Xu JJ, Yin WT. An iterative regularization method for total variation-based image restoration. Multiscale Model Simul 2005;4:460–489.

27. Zhang H, Cheng L, Li J. Reweighted minimization model for MR image reconstruction with split Bregman method. Sci China Inf Sci 2012;55:2109–2118.

28. Smith DS, Welch EB.Non-sparse phantom for compressed sensing MRI reconstruction. In Proceedings of the 19th Annual Meeting of ISMRM, Montreal, Quebec, Canada, 2011. Abstract 2845.

29. Michailovich O, Rathi Y, Dolui S. Spatially regularized compressed sensing for high angular resolution diffusion imaging. IEEE Trans Med Imaging 2011;30:1100–1115.

30. Ye X, Chen Y, Lin W, Huang F. Fast MR image reconstruction for partially parallel imaging with arbitrary k-space trajectories. IEEE Trans Med Imaging 2011;30:575–585.

31. Wech T, Lygate C, Neubauer S, Kostler H, Schneider J. Highly accelerated cardiac functional MRI in rodent hearts using compressed sensing and parallel imaging at 9.4T. J Cardiovasc Magn Reson 2012; 14(Suppl 1):P65.

32. Wech T, Medway D, Lygate C, Neubauer S, Kostler H, Schneider J. Accurate infarct-size measurements from accelerated, compressed sensing reconstructed cine-MRI images in mouse hearts. J Cardiovasc Magn Reson 2012;14(Suppl 1):P57.

33. Motaal AG, Coolen BF, Abdurrachim D, Castro RM, Prompers JJ, Florack LMJ, Nicolay K, Strijkers GJ. Accelerated high-frame-rate mouse heart cine-MRI using compressed sensing reconstruction. NMR Biomed 2013;26:451–457.

34. Shi Y, Chang Q. Efficient algorithm for isotropic and anisotropic total variation deblurring and denoising. J Appl Math 2013;2013:14.

35. Wang YL, Yang JF, Yin WT, Zhang Y. A new alternating minimization algorithm for total variation image reconstruction. SIAM J Imaging Sci 2008;1:248–272.

36. van den Berg E, Friedlander MP. Probing the pareto frontier for basis pursuit solutions. SIAM J Sci Comput 2008;31:890–912.

37. Becker S, Bobin J, Candes EJ. NESTA: a fast and accurate first-order method for sparse recovery. SIAM J Imaging Sci 2009;4:1–39.

38. Abascal J, Chamorro-Servent J, Aguirre J, Arridge S, Correia T, Ripoll J, Vaquero JJ, Desco M. Fluorescence diffuse optical tomography using the split Bregman method. Med Phys 2011;38:6275– 6284.

39. Montesinos P, Abascal JFPJ, Chamorro J, Chavarrias C, Benito M, Vaquero JJ, Desco M.High-resolution dynamic cardiac MRI on small animals using reconstruction based on split Bregman methodology. In Proceedings of the Nuclear Science Symposium and Medical Imaging Conference (NSS/MIC), Valencia, California, USA, 2011. p 3462– 3464.

40. Cai J, Osher S, Shen Z. Split Bregman methods and frame based image restoration. Multiscale Model Simul 2010;8:337–369.

41. Hankiewicz JH, Goldspink PH, Buttrick PM, Lewandowski ED. Principal strain changes precede ventricular wall thinning during transition to heart failure in a mouse model of dilated cardiomyopathy. Am J Physiol Heart Circ Physiol 2008;294:H330–H336.

42. Starck JL, Elad M, Donoho DL. Image decomposition via the combination of sparse representations and a variational approach. IEEE Trans Image Process 2005;14:1570–1582.

43. Bilen C, Selesnick IW, Wang Y, Otazo R, Kim D, Axel L, Sodickson DK.On compressed sensing in parallel MRI of cardiac perfusion using temporal wavelet and TV regularization. 2010 IEEE International Conference on Acoustics Speech and Signal Processing (ICASSP) 2010:630–633.